Fe_3O_4-CS-L: a magnetic core-shell nano adsorbent for highly efficient methyl orange adsorption

Shuangzhen Guo, Jian Zhang, Xianlong Li, Fan Zhang and Xixi Zhu

ABSTRACT

A novel core-shell bio-adsorbent was fabricated by using biological materials for removing methyl orange (MO) from aqueous solution. The structure characteristics results of scanning electron microscopy (SEM), Fourier transform infrared spectrometry (FT-IR), thermo-gravimetric analysis (TGA), vibrating sample magnetometer (VSM), and Brunauer–Emmett–Teller (BET) shows that Fe_3O_4-CS-L has been successfully prepared. The effects of contact time, pH, temperature and initial concentration were explored. The results suggested pH was a negligible factor in adsorption progress. Kinetic studies showed that the experiment data followed pseudo-second-order model. Boyd mode suggested that external mass transfer showed a rather weak rate control for MO adsorption onto Fe_3O_4-CS-L. Equilibrium studies showed that isotherm data were the best described by Langmuir model. The maximum adsorption capacity of MO estimated to be 338.98 mg/g at 298 K. Moreover, the adsorption capacity of Fe_3O_4-CS-L can keep about 74% in the fifth adsorption–regeneration cycle. Thus, the Fe_3O_4-CS-L could be a kind of promising material for removing MO from wastewater.

Key words | adsorption, bio-adsorbent, L-arginine and chitosan, methyl orange

Shuangzhen Guo (corresponding author)
Xianlong Li
Fan Zhang
School of Environmental Science and Engineering,
Tianjin University,
92 Weijin Road, Tianjin 300072,
China
E-mail: *jieliu0619@163.com*

Jian Zhang
State Key Laboratory of Pollution Control and Resource Reuse, School of Environment,
Nanjing University,
163 Xianlin Avenue, Nanjing 210023,
China

Xixi Zhu
College of Chemistry and Environmental Engineering,
Shandong University of Science and Technology,
579 Qianwangang Road, Qingdao 266590,
China

INTRODUCTION

In recent years, water pollution has caught social and academic attention. Dye and heavy metals pollution are the two most common pollution scenarios in water pollution. More than 7×10^5 tones commercial dyes are produced per year for coloring product (Sen *et al.* 2010). Among them, the consumption of dyes are more than 10,000 t/year in the textile industry and over 100 t/year of dyes is discharged into environment (Yagub *et al.* 2012). It is very difficult to degradation for most of dyes, due to complex composition, stable chemical properties and high chemical oxygen consumption. Hence, the treatment of dye wastewater are attracted more and more attention.

Various of techniques have been used to deal with dye wastewater such as membrane filtration (Alventosa *et al.* 2012), aerobic or anaerobic treatment (Hosseini *et al.* 2011), electrochemical treatment (Körbahti *et al.* 2011), coagulation–flocculation (García *et al.* 2008) and adsorption methods (Tang *et al.* 2013; Zhang *et al.* 2014). Among of them, more and more attention is given to adsorption because of its cost-effective and easy to operate. Conventionally, inorganic nanoparticle (Muthukumaran *et al.* 2016; Wang *et al.* 2016), zeolites (Faki *et al.* 2008), bentonite (Weng & Pan 2007; Lian *et al.* 2009) and active carbon (Jiang *et al.* 2015) were reported to deal with dye wastewater. As one coin has two sides, these adsorbents also have their own shortcomings, such as separation inconvenience, high cost of raw materials and low adsorption capacity. Hence, it is the design aim of adsorbent which own the advantages of high adsorption capacity, low cost of raw materials and facile separation.

Chitosan, as a biopolymer, can be extracted from chitin and has abundant sources (Wu *et al.* 2016). Due to abundant amino groups and hydroxy groups, which were located on the carbon skeleton of chitosan, chitosan have potential for removing dye from wastewater by adsorption method. Recently, magnetic adsorbents have been widely used to remove dyes and heavy metals from aqueous solution, because it can enhance the separation rate (Asfaram *et al.* 2015; Habila *et al.* 2016). Chitosan was often used to combine with magnetic materials to prepare magnetic core-shell nanoparticles which consist of an iron oxide core and chitosan shell. Li has investigated that 3-chloro-2-hydroxypropyl trimethyl ammonium modified chitosan magnetic composite was used to remove methyl orange

doi: 10.2166/wst.2017.602

(MO) from aqueous solution (Li *et al.* 2016). Elwakeel also discussed magnetic chitosan for the removal of reactive black 5 from wastewater (Elwakeel 2009). However, chitosan is not stable and soluble in acidic solution and its ability to adsorb dye is still insufficient, which limits its future application in the treatment of dye wastewater. In modifying the chitosan shells by chemical modification, it not only can solve the instability and acid resistance, but also can achieve a specific function, such as large adsorption capacity and bioseparation (Reddy & Lee 2013). Various dyes could be adsorbed by some specific interactions such as hydrogen bond and electrostatic attraction (Sakkayawong *et al.* 2005). Various functional groups could be flexibly grafted onto chitosan for effective adsorption of dyes (Li *et al.* 2016). *L*-arginine with amino groups and carboxyl groups has good water solubility. It could improve stability and adsorption capacity of chitosan, if chitosan was modified by *L*-arginine (Arash *et al.* 2016).

In this paper, a novel magnetic core-shell adsorbent was prepared by grafting chitosan and *L*-arginine on the surface of Fe_3O_4. This magnetic adsorbent was developed for the adsorption of MO from aqueous solution. Combining functionalities of magnetism and biopolymer, magnetic core-shell chitosan nanoparticles show fast separation properties and high adsorption capacity.

MATERIALS AND METHODS

Materials

Potassium iodide, $FeSO_4{\cdot}7H_2O$, *L*-arginine, sodium hydroxide, sodium thiosulfate, acetone, NaOH, HNO_3 and ethanol were purchased from Sinopharm Chemical Reagents Corp. (Shanghai, China). Chitosan, glutaraldehyde and epoxy chloropropane were Aladdin products (Shanghai, China). In this study, the water is deionized water and all reagents were of analytical grade.

Synthesis of magnetic composite

Fe_3O_4 is prepared by traditional hydrothermal synthesis method (Guo *et al.* 2017).

Chitosan (1.0 g) was dissolved in acetic solution (3%, 100 mL), then Fe_3O_4 (1.0 g) were added in the chitosan solution. Glutaraldehyde (8.0 mL) was dropwise added into the mixed solution under stirring at 333 K for 2 h (Fan *et al.* 2012). The residues were washed with deionized water and ethanol until pH was about 7. Afterward, the residues were dissolved in acetone (100 mL) and stirred to form a suspension. Epichlorohydrin (5.0 mL) was added dropwise to suspensions. This suspension was stirred for 24 h at 303 K (Kuang *et al.* 2013).

L-arginine (6.0 g) was dissolved in dimethyl formamide (50 mL) and then slowly dropped into the reaction, K_2CO_3 (3.0 g) which have roasted under high temperature and KI (0.05 g) were added in solution and the mixture was reflux at 338 K for 12 h. The residues were washed with distilled water, ethanol and acetone in turn. The residue was dried at 333 K under vacuum condition. The structure diagram of Fe_3O_4-CS-L is shown in Figure 1.

Characterization

X-ray powder diffraction (XRD) results were obtained on Rigaku IV (Rigaku, Japan). Scanning electron microscope (SEM) images were obtained on IGMA (Carl Zeiss, Germany). The hysteresis loops were tested by a vibrating sample magnetometer (LDJ 9600, USA). Fourier transform infrared (FT-IR) spectra were gained by infrared spectrometer (Thermo Nicolet 380, USA). The thermogravimetric analysis (TGA) result was obtained by thermogravimetric analyzer (SDTA851, Swit). The concentration of MO was determined with double beam ultraviolet (UV)–vis spectrophotometer (TU-1901, China).

Batch adsorption experiments

Batch adsorption experiments were shocked on water bath equipment (Bote Ltd, China) with a shock speed of

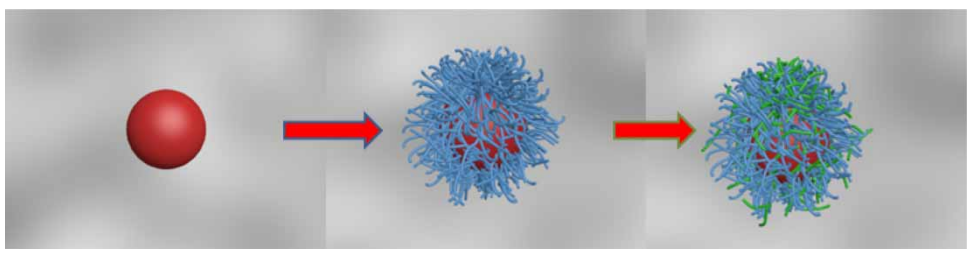

Figure 1 | The structure diagram of Fe_3O_4-CS-L.

300 rpm, Fe_3O_4-CS-L (0.1 g) was added in 100 mL different concentrations of MO solution. NaOH(0.1 mol/L) or HNO_3(0.1 mol/L) solution was used to adjust the pH of the aqueous solutions. The adsorption capacity of Fe_3O_4-CS-L at any time and equilibrium are calculated according to the formula:

$$q_t = \frac{(C_0 - C_t) \cdot V}{W} \quad (1)$$

$$q_e = \frac{(C_0 - C_e) \cdot V}{W} \quad (2)$$

The removal percentage (%) was calculated as follows:

$$\eta = \frac{C_0 - C_e}{C_0} \times 100\% \quad (3)$$

where C_0 (mg/L), C_t (mg/L) and C_e (mg/L) represent the initial MO concentration, at time t and the equilibrium time, respectively; V on behalf of the volume of the MO solution (mL) and W is the amount of adsorbent (mg).

RESULTS AND DISCUSSION

Characteristics of the prepared Fe_3O_4-CS-L

Figure 2 shows the microtopography of Fe_3O_4 and Fe_3O_4-CS-L. From Figure 2, we found that Fe_3O_4 and Fe_3O_4-CS-L showed irregular polyhedron morphologies. Moreover, the radius of Fe_3O_4-CS-L was larger than that of Fe_3O_4. The agglomeration of Fe_3O_4 was more serious than Fe_3O_4-CS-L.

Figure 3 shows FT-IR spectra of Fe_3O_4, Fe_3O_4-CS and Fe_3O_4-CS-L. As for Fe_3O_4, Fe_3O_4-CS and Fe_3O_4-CS-L, the absorption peak in 568 cm^{-1} appears which related to Fe-O stretching vibrations. As for magnetic chitosan, a broad weak absorption peak in the range of 2,600–3,300 cm^{-1} appears which corresponds to N-H and O-H stretching vibrations, the new peaks at 2,030 cm^{-1} are ascribed to the ammonium salt feature peaks, the peaks at 1,210–1,010 cm^{-1} are related to the C-O and C-N stretching vibrations. It proved that chitosan has been grafted on surface of magnetic Fe_3O_4 with the help of glutaraldehyde. When *L*-arginine is grafted on magnetic chitosan, a new band at 1,750 cm^{-1} and 1,690–1,640 cm^{-1} due to C = O and C = N stretching vibration in *L*-arginine. In addition, the obviously strengthened peak at 1,073 cm^{-1} in Fe_3O_4-CS-L, which is related to the reaction between acyl chloride (in Fe_3O_4-CS) and amino (in *L*-arginine). The FT-IR spectra results proved that Fe_3O_4-CS-L has been prepared successfully.

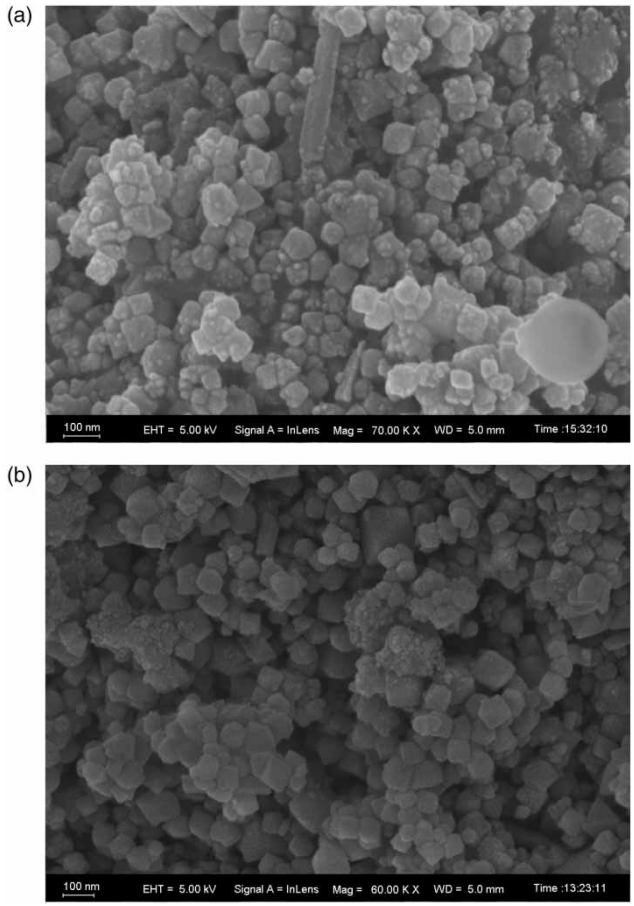

Figure 2 | SEM morphology of Fe_3O_4 (a) and Fe_3O_4-CS-L (b).

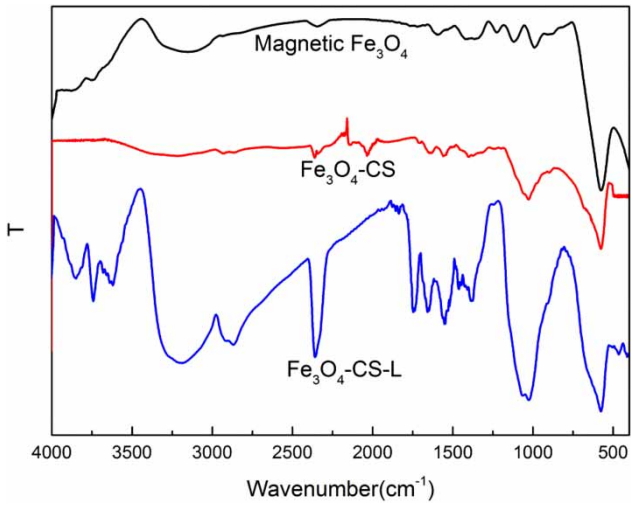

Figure 3 | The IR spectra of Fe_3O_4, Fe_3O_4-CS and Fe_3O_4-CS-L.

Thermogravimetric results of Fe_3O_4, Fe_3O_4-CS and Fe_3O_4-CS-L are shown in Figure 4. From Figure 4, it can be found that there were two decomposed quantities of 3.67% from 55 °C to 122 °C, and of 3.27% from 601 °C to 708 °C in magnetic Fe_3O_4 thermogravimetric curve, corresponding to adsorbed water and to condensation of the iron oxide hydroxyl. For Fe_3O_4-CS, there is an additional mass loss step of 44.1% from 135 °C to 715 °C attributed to the chitosan grafted on surface of magnetic Fe_3O_4. As for Fe_3O_4-CS-L, it showed four decomposed quantities of 4.15% from 55 °C to 120 °C, of 31.46% from 122 °C to 352 °C, of 7.19% from 352 °C to 419 °C, and of 15% from 419 °C to 516 °C, which are related to adsorbed water, amino, carboxyl and hydroxyl in chitosan carbon skeleton thermal decomposition. The TGA results showed that the grafted chitosan and *L*-arginine were calculated to be approximately 58.41% for the total mass of Fe_3O_4-CS-L.

Figure S1 (available with the online version of this paper) shows Brunauer–Emmett–Teller (BET) results of Fe_3O_4-CS-L. Adsorption measurements were performed under the same conditions, followed by desorption measurements. According to International Union of Pure and Applied Chemistry (IUPAC) classification, the isotherm is a type III and the BET surface area is 3.63 m^2/g.

The magnetization of Fe_3O_4 and Fe_3O_4-CS-L were investigated with a vibrating sample magnetometer (VSM). From Figure S2 (available online), the saturation magnetization (M_s) value of Fe_3O_4 and Fe_3O_4-CS-L were 57.6 and 14.1 emu/g, respectively. Although magnetization strength decreased after grafting chitosan and *L*-arginine, it could be concluded that the separation of Fe_3O_4-CS-L in aqueous solution could be controlled by electromagnet with convertible magnetic field.

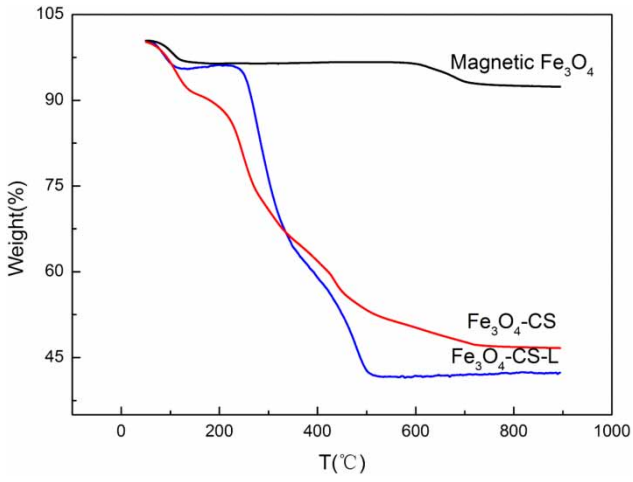

Figure 4 | Thermogravimetric curve of magnetic Fe_3O_4, Fe_3O_4-CS and Fe_3O_4-CS-L.

Adsorption experiments

Effect of initial MO concentration

Figure 5 shows the effect of initial MO concentration on adsorption capacity. As shown in Figure 5, the equilibrium adsorption capacity increases while the removal efficiencies drop rapidly with increases of initial MO concentrations from 100 mg/L to 500 mg/L. At range of 500–700 mg/L, the equilibrium adsorption capacity keeps in a stable value (240 mg/g). This is due to the fact that the functional groups which were located on the surface of Fe_3O_4-CS-L tend to saturate with increases of MO concentration and it reached saturation at a concentration of 500 mg/L. So, the equilibrium adsorption capacity remains constant in the range of 500–700 mg/L. Thus, the optimal MO concentration was confirmed at 500 mg/L for the following experiments.

Effect of pH

As we all know, there are two main structures of MO at different pH values. It is present as a quinone type at a lower pH (under acidic conditions), while it is rearranged into azo structure at a higher pH (Zhu *et al.* 2010). The rearrangement of MO is shown below:

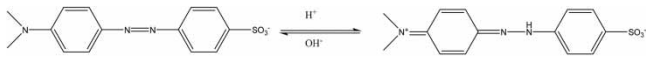

The adsorption capacity was certainly influenced by the change of structure of MO, so it is essential to explore the effect of pH changes on adsorption capacity. Figure 6

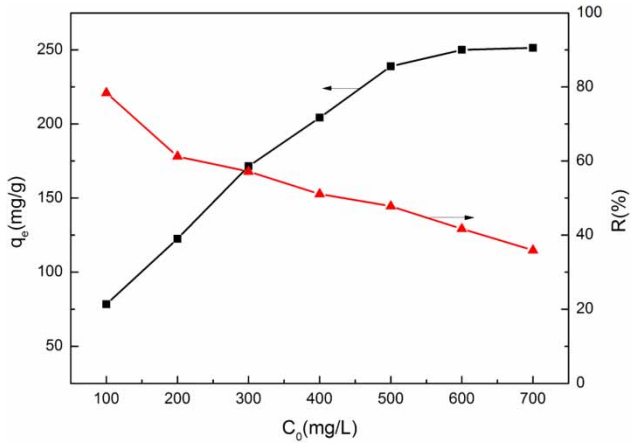

Figure 5 | Effect of initial concentration of MO on adsorption removal efficiency and adsorption capacity (Experiment condition: pH = 3, T = 298 K, contact time is 50 min).

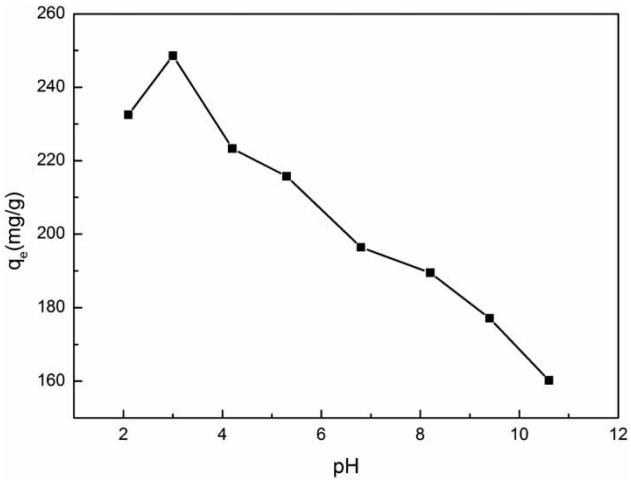

Figure 6 | Effect of pH on the adsorption capacity (Experiment condition: $C_0 = 500$ mg/L, T = 298 K, contact time is 50 min).

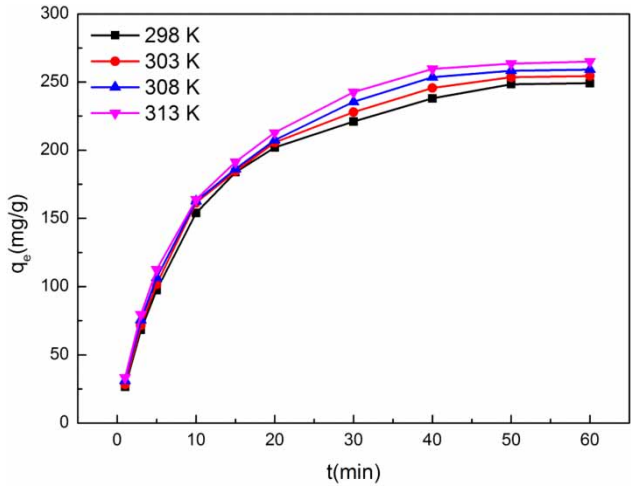

Figure 7 | Effect of contact time and temperature on the adsorption removal efficiency of MO (Experiment condition: pH = 3, $C_0 = 500$ mg/L, T = 298 K).

shows that the change of adsorption capacity was investigated at varying pH values 2–11. As shown in Figure 6, the adsorption capacity increased from 231 mg/g to 252 mg/g with increases of pH from 2 to 3. The maximum value of adsorption capacity was reach at pH = 3, and the adsorption capacity decreases at range of 3–11.

The dissociation constant of MO is 3.46, it means the structure of MO is presented as quinone at the pH<3.0, the two main active sites of quinone structure are sulfinyl and amino groups. The –S = O group can be served as the electron pair acceptor and form regular hydrogen bonding with the amino group (–NH_2) of Fe_3O_4-CS-L surface, while the –NH group can be served as the electron pair donor and form regular hydrogen bonding with the carboxyl group (–COOH) in Fe_3O_4-CS-L composite. The hydrogen bonding between MO and Fe_3O_4-CS-L may result in the presence of large adsorption capacity at lower pH. With increases of pH from 3 to 11, the adsorption capacities of MO drop gradually. When the pH is increased, quinone structure of MO is gradually transformed into its azo structure. Azo structure of MO only has one reaction site –S = O can form regular hydrogen bonding and the hydrogen bonding between MO and Fe_3O_4-CS-L is reduced, which leads to the decrease of adsorption capacity (Liu *et al.* 2015). In addition, there is competition repulsion existence between MO anions and OH^-, which lead to the decrease in MO adsorption (Subbaiah & Kim 2016).

Effects of contact time and temperature

Contact time and temperature are two of the most important factors which can affect adsorption progress. As shown in Figure 7, the effect of temperature and contact time on adsorption MO. From Figure 7, we can find that the adsorption capacity is increasing with increases of contact time within 50 min and then the adsorption capacity keep a stable value beyond 50 min. In addition, the adsorption capacity is increasing with increases of temperature from 298 K to 313 K, it also proved that the adsorption progress is endothermic in nature. According to the above results, 50 min was considered to equilibrium time in batch adsorption experiments. There is no significant change of adsorption capacity from 298 K to 313 K, so the temperature is determined as 298 K in the following experiment.

Adsorption kinetic

The mechanism of adsorption progress can be investigated by fitting kinetic model. Considerable research efforts have been devoted to three kinetic models (pseudo-first-order kinetic model, pseudo-second-order kinetic model and intraparticle diffusion model) to describe adsorption progress mechanism.

The equation of pseudo-first-order model and pseudo-second-order are represented as follows:

$$\log(q_e - q_t) = \log q_e - \frac{K_1 t}{2.303} \tag{4}$$

$$\frac{t}{q_t} = \frac{1}{K_2 (q_e)^2} + \frac{t}{q_e} \tag{5}$$

where q_t and q_e (mg/g) are the adsorption capacity for MO adsorbed at any time t and at equilibrium time. K_1 (min^{-1}) is

the rate constant of the pseudo-first-order and K_2 (min^{-1}) is the rate constant of the pseudo-second-order. t is contact time. The data of the fitted models by use of these equations are shown in Table 1 and Figure S3 (available online).

The R^2 values of the pseudo-second-order model are higher than the pseudo-first-order model. In others word, the pseudo-second-order model is more suitable for describing the adsorption behavior of MO on Fe_3O_4-CS-L, indicating the sort of adsorption is chemical adsorption.

As we all know, the adsorption process can be divided into three stages: (1) MO was moved from the bulk solution to the boundary layer; (2) diffuse through the boundary layer to the surface of adsorbent; (3) adsorb onto an active site. Intraparticle diffusion model was often used to describe the contribution of intraparticle diffusion to rate control step. The intraparticle diffusion model can be described as follows:

$$q_t = K_i t^{0.5} + C \tag{6}$$

where C is a constant and K_i is the rate constant. The data of the fitted models by using of these equations are shown in Table 2 and Figure S4 (available online). It is obvious that the $q_t - t^{0.5}$ polts can be divided into three distinct regions. The external mass transfer is related to the first linear portion. The intraparticle diffusion is related to the second linear portion. The adsorption–desorption equilibrium is related to the third linear portion. It is important to highlight that the time of intraparticle diffusion is decreasing with increases of temperature, indicating temperature would influence the diffusion rate in intraparticle diffusion stage. Table 2 data show that the second linear portion does not get through the origin point from 293 to 308 K, meaning that intraparticle diffusion is not the only rate-limiting step.

Boyd mode was used to distinguish the rate control step in adsorption between intraparticle diffusion and mass transfer. Boyd mode can been described as follows:

$$B_t = -\ln\left(1 - \frac{q_t}{q_e}\right) - 0.4977 \tag{7}$$

where q_t and q_e are the adsorption capacity of MO adsorbed on the adsorbent (mg/g) at any time t (min) and at equilibrium time (min), respectively. As shown in Figure S5 (available online), the fitted linear (298–313 K) do not pass through the origin point, confirming the existence of external mass transfer in the whole adsorption process. What is more, it is clear that there are two parts in the fitting line, implying that external mass transfer shows a rather weak rate control for MO adsorption onto Fe_3O_4-CS-L materials (Ma *et al.* 2012).

Table 1 | Dynamic parameters for the adsorption of MO onto Fe_3O_4-CS-L

	Prsudo-first-order			Prsudo-second-order		
T(K)	K_1	q_e	R^2	K_2	q_e	R^2
298	0.075	219.28	0.991	3.60×10^{-4}	292.40	0.9991
303	0.081	233.35	0.988	3.66×10^{-4}	297.62	0.9992
308	0.092	259.42	0.971	3.74×10^{-4}	302.11	0.9990
313	0.097	272.27	0.966	3.94×10^{-4}	302.75	0.9991

Table 2 | Parameters of the Intraparticle diffusion model for the adsorption of MO onto Fe_3O_4-CS-L

	First linear portion			Second linear portion		
T(K)	K_{d1}	C_1	R_1^2	K_{d2}	C_2	R_2^2
298	58.923	−33.230	0.9995	19.951	110.036	0.9840
303	61.543	−34.377	0.9990	21.513	106.308	0.9652
308	60.776	−29.622	0.9999	27.335	83.003	0.9864
313	60.512	−25.688	0.9977	27.904	86.055	0.9818

Adsorption isotherms

Adsorption isotherms can be expressed as functional equations which describes the amount of metal ions adsorbed per unit mass of the adsorbent and the concentration of metal ions in bulk solution under equilibrium conditions. The three most common adsorption isotherm for describing solid–liquid sorption systems are Langmuir, Freundlich and Temkin isotherms The equation for the Langmuir (8), Freundlich (9) and Temkin (10) isotherm are as follows:

$$\frac{C_e}{q_e} = \frac{1}{q_m \cdot K_L} + \frac{C_e}{q_m} \tag{8}$$

$$\log q_e = \log K_F + \frac{\log C_e}{n} \tag{9}$$

$$q_e = \frac{RT}{b} \ln A + \frac{RT}{b} \ln C_e \tag{10}$$

where C_e and q_e are the equilibrium concentration of the metal ions (mg/L) and the adsorption capacity (mg/g), respectively. The maximum adsorption capacity of

adsorbents (mg/g) and the adsorption constant (L/mg) in Langmuir mode are represented by q_m and K_L. K_F is related to the adsorption capacity. n is the Freundlich constants which positive relate to the adsorption strength. b and A are the constant related to the adsorption heat (J/mol) and isothermal adsorption constant of Temkin, respectively. T is the temperature (K). R is the ideal gas constant (8.314 J/mol K).

The fitted data for MO adsorption on Fe_3O_4-CS-L were obtained as shown in Figure S6 (available online) and Table 3. As shown in Table 3, R^2 of Langmuir isotherm is greater than the Freundlich and Temkin model, it means that the Langmuir isotherm model is more suitable for the adsorption process. In other words, the adsorption process is a single adsorption and active sites evenly distributed on the surface of Fe_3O_4-CS-L.

In Langmuir mode, the degree of appropriate of adsorbent towards MO is predicted from the values of separation factor constant (R_L), which is shown as follows:

$$R_L = \frac{1}{1 + K_L C_0} \tag{11}$$

where K_L is the Langmuir isotherm constant (L/mg). C_0 is the initial MO concentration (mg/L). The value of R_L shows that the adsorption MO on Fe_3O_4-CS-L is favorable ($0 < R_L < 1$) or irreversible ($R_L = 0$), linear ($R_L = 1$), unfavorable ($R_L > 1$) (Ren *et al.* 2013). As shown in Table 3, the values of R_L were between 0.3 and 0.7, suggesting favorable adsorption of the MO on Fe_3O_4-CS-L.

Possible adsorption mechanism of MO by Fe_3O_4-CS-L

Figure 8 shows the conceptual model for the MO removal mechanism by Fe_3O_4-CS-L. MO is represented as the quinone structure in the solution when the pH is lower than 3.46. The secondary amino groups and sulfinyl on the surface of the quinone structure of MO can form hydrogen bonds with the carboxyl and amino groups on the surface of Fe_3O_4-CS-L, respectively. In addition, the electrostatic force is a factor that cannot be ignored in the adsorption process. There is electrostatic repulsion that exists between N^+ group in quinone type structure of MO and $-NH_3^+$ group of Fe_3O_4-CS-L surface. With increasing the value of pH, the quinone structure of MO was gradually transformed into azo structure, the hydrogen bond between –NH and –COOH becomes gradually weakened and the electrostatic repulsion between N^+ group in quinone type structure of MO and $-NH_3^+$ group of Fe_3O_4-CS-L surface also become gradually weakened. As shown in Figure 8, the adsorption capacity gradually decreased with the increase of pH value, suggesting that the influence of hydrogen bond is much larger than electrostatic interaction on MO adsorption progress. What is more, the Van der Waals force enhances as the unit surface charge density increase, which suppress the adsorption capacity of MO in Fe_3O_4-CS-L.

Removal of MO in real wastewater samples

The adsorption progress was often influenced by various kinds of factors such as ion strength and coexistence organic molecules. In order to confirm the adsorption capacity of Fe_3O_4-CS-L under real conditions, removal of MO in real wastewater samples were investigated. The sample of wastewater was obtained from Ruibei printing and dyeing mill (Jiangsu, China). Nylon membrane (0.45 μm) was used to removal contamination particles of samples. Table 4 shows the main components of the sample. Figure S7 (available online) shows that the effect of contact time on MO adsorption under real conditions. From Figure S7, it can be found that the adsorption equilibrium contact time was 60 min, which was larger than the adsorption time in the simulated solution. Moreover, the adsorption capacity of Fe_3O_4-CS-L is 145 mg/g, which is reduced by 23% comparing to the adsorption capacity in

Table 3 | Langmuir, Freundlich and Temkin isotherm model parameters for MO adsorption on Fe_3O_4-CS-L

	Langmuir				Freundlich			Temkin		
T(K)	q_m	K_L	R_L	R^2	K_F	n	R^2	A	b	R^2
298	338.98	0.0031	0.315–0.762	0.997	6.668	1.816	0.979	0.026	31.09	0.994
303	353.36	0.0030	0.323–0.769	0.999	6.486	1.790	0.977	0.025	30.53	0.992
308	363.64	0.0029	0.330–0.775	0.997	6.389	1.772	0.982	0.025	30.25	0.991
313	374.53	0.0027	0.346–0.787	0.998	6.310	1.757	0.980	0.024	29.99	0.995

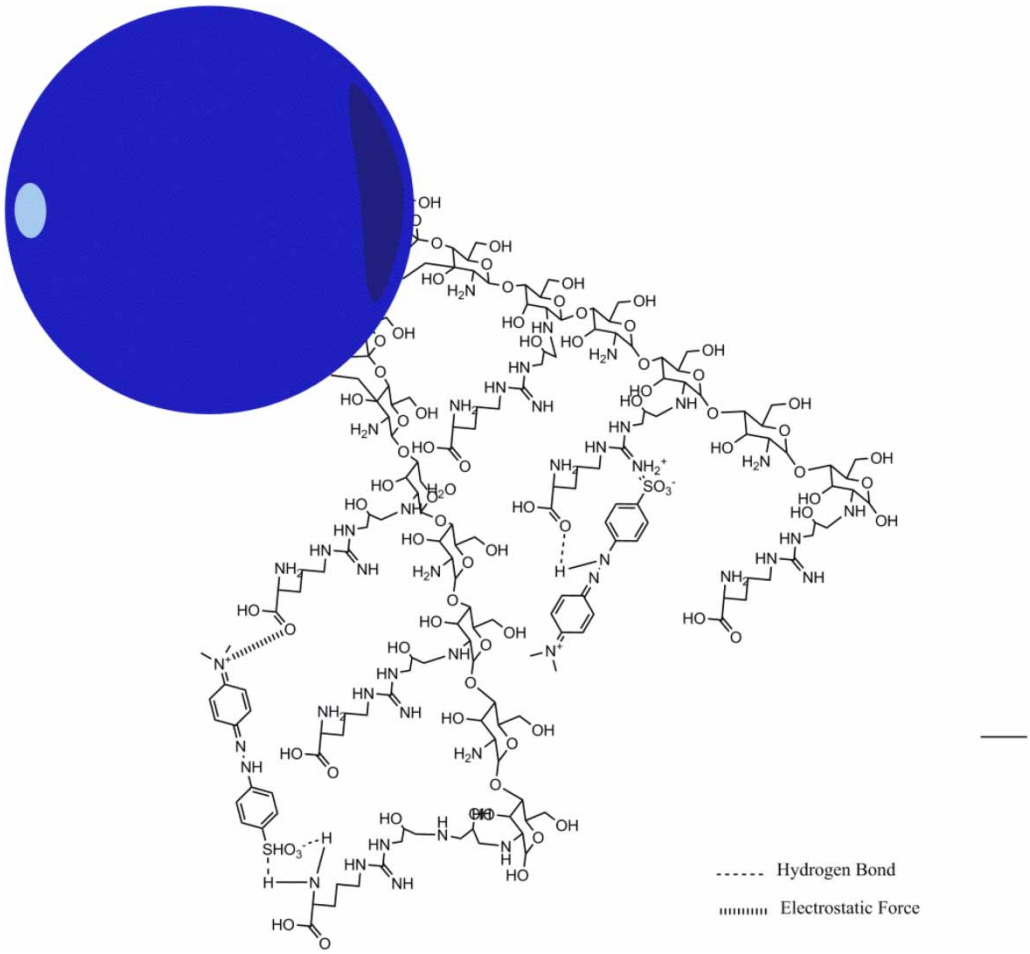

Figure 8 | The conceptual model for the MO removal mechanism.

Table 4 | The main components of the water samples

Main components	pH	MO (mg/L)	Amine base class (mg/L)	Salts contain (%)
Concentration	8.3	431	76	19.2

the simulated solution at pH = 8.3. It can be explained that there are a variety of co-existing ions present in the actual wastewater. Azo structure of MO could be combined with organic groups by hydrogen bonding, resulting in a larger molecular structure and increased resistance to diffusion. In addition, azo structure with negative charged can interact with the coexistence of cations by electrostatic attraction, thereby reducing the interaction with Fe_3O_4-CS-L, which also results in slower adsorption rates and lower adsorption capacity. Moreover, the coexistence of cations can also interact with the functional groups on Fe_3O_4-CS-L, resulting in a decrease in hydrogen bonding between Fe_3O_4-CS-L and MO. This also leads to a decrease in adsorption capacity.

Regeneration of Fe_3O_4-CS-L

It is a very important feature for adsorbent in industrial applications. Figure S8 (available online) shows desorption and reusability studies of Fe_3O_4-CS-L in 1 mol/L HNO_3. The adsorption capacity of Fe_3O_4-CS-L can keep about 74% in the fifth adsorption-regeneration cycle, suggesting that this material has the prospect of industrial applications.

Comparison with other adsorbents

Table 5 shows the maximum adsorption capacities of different types of adsorbent. It was found that the adsorption capacity of Fe_3O_4-CS-L was greater than other adsorbent

Table 5 | Comparison of MO adsorption capacity among different adsorbents

Adsorbent	q_m(mg/g)	References
γ-Fe_2O_3/2C nanocomposite	42.34	Istratie *et al.* (2016)
Mesoporous NiO microspheres	137.00	Jia *et al.* (2014)
CuO/NaA zeolite	79.49	Mekatel *et al.* (2015)
Activated carbon/$NiFe_2O_4$	182.82	Jiang *et al.* (2015)
Chitosan biomass	29.00	Allouche *et al.* (2015)
Maghemite/chitosannanocomposite films	29.41	Jiang *et al.* (2012)
Immobilized PANI/glass	93.0	Haitham *et al.* (2015)
Activated clay	16.78	Ma *et al.* (2013)
Fe_3O_4-CS-L	338.98	In this work

for MO adsorption, suggesting that Fe_3O_4-CS-L can be used as an efficient adsorbent of MO.

CONCLUSION

In summary, a novel magnetic bio-adsorbent was prepared by use of chitosan and *L*-arginine. The SEM and FT-IR results show that chitosan and *L*-arginine have been grafted on surface of magnetic Fe_3O_4 and TGA results future confirms that chitosan and *L*-arginine account for 58.4% of total mass. pH plays an important role in adsorption progress and the optimum pH for adsorption is 3. The adsorption capacity of Fe_3O_4-CS-L has reached saturated at a concentration of 500 mg/L. Kinetic studies show that the experiment data can be better described by pseudo-second-order model, not pseudo-second-order model. Boyd mode shows that external mass transfer shows a rather weak rate control for MO adsorption onto Fe_3O_4-CS-L. Equilibrium studies show that isotherm data were best described by Langmuir model. The maximum adsorption capacity of MO estimated to be 338.98 mg/g at 298 K and pH 3.0. The adsorption capacity of Fe_3O_4-CS-L can keep about 74% in the fifth adsorption-regeneration cycle, indicating that it has potential for industrial applications.

REFERENCES

Allouche, F. N., Yassaa, N. & Lounici, H. 2015 Sorption of methyl orange from aqueous solution on chitosan biomass. *Procedia Earth and Planetary Science* **15**, 596–601.

Alventosa, D. E., Barredo, D. S., Alcaina, M. I. & Iborra-Clar, M. I. 2012 Ultrafiltration technology with a ceramic membrane for reactive dye removal: optimization of membrane performance. *Journal of Hazardous Materials* **209–210**, 492–500.

Arash, D., Ramin, N., Mohammad, R. G., Khoobi, M., Nazmara, S. & Mahvi, A. H. 2016 Efficient adsorption of both methyl orange and chromium from their aqueous mixtures using a quaternary ammonium salt modified chitosan magnetic composite adsorbent. *Journal of Magnetism and Magnetic Materials* **154**, 179–189.

Asfaram, A., Ghaedi, M., Goudarzi, A., Soylak, M. & Langroodi, S. M. 2015 Magnetic nanoparticle based dispersive microsolid-phase extraction for the determination of malachite green in water samples: optimized experimental design. *New Journal of Chemistry* **39** (12), 9813–9823.

Elwakeel, K. Z. 2009 Removal of Reactive Black 5 from aqueous solutions using magnetic chitosan resins. *Journal of Hazardous Materials* **167**, 382–392.

Faki, A., Turan, M., Ozdemir, O. & Tura, A. Z. 2008 Analysis of fixed-bed column adsorption of reactive yellow 176 onto surfactant-modified zeolite. *Industrial and Engineering Chemistry Research* **47**, 6999–7004.

Fan, L. L., Luo, L. N., Li, X. J., Lu, F. G., Qiu, H. M. & Sun, M. 2012 Fabrication of novel magnetic chitosan grafted with graphene oxide to enhance adsorption properties for methyl blue. *Journal of Hazardous Materials* **215–216**, 272–279.

García, M. J., Domènech, X., García-Hortal, J. A., Torrades, F. & Peral, J. 2008 The testing of several biological and chemical coupled treatments for Cibacron Red FN-R azo dye removal. *Journal of Hazardous Materials* **154** (1–3), 484–490.

Guo, S. Z., Jiao, P. P., Dan, Z. G., Duan, N., Chen, G. Y. & Zhang, J. 2017 Preparation of *L*-arginine modified magnetic adsorbent by one-step method for removal of Zn(II) and Cd(II) from aqueous solution. *Chemical Engineering Journal* **317**, 999–1011.

Habila, M. A., AL Otheman, Z. A., El-Toni, A. M. & Yaghoobia, F. 2016 Synthesis and application of Fe_3O_4@SiO_2@TiO_2 for photocatalytic decomposition of organic matrix simultaneously with magnetic solid phase extraction of heavy metals prior to ICP-MS analysis. *Talanta* **154**, 539–547.

Haitham, K., Razak, S. & Nawi, M. A. 2015 Kinetics and isotherm studies of methyl orange adsorption by a highly recyclable immobilized polyaniline on a glass plate. *Arabian Journal of Chemistry* doi:http://dx.doi.org/10.1016/j.arabjc.2014.10.010 (in press).

Hosseini, K. E., Alavi, M. R. & Hashemi, S. H. 2011 Post-treatment of anaerobically degraded azo dye Acid Red 18 using aerobic moving bed biofilm process: enhanced removal of aromatic amines. *Journal of Hazardous Materials* **195**, 147–154.

Istratie, R., Stoia, M., Păcurariu, C. & Locovei, C. 2016 Single and simultaneous adsorption of methyl orange and phenol onto magnetic iron oxide/carbon nanocomposites. *Arabian Journal of Chemistry* DOI: 10.1016/j.arabjc.2015.12.012.

Jia, Z., Liu, J., Wang, Q., Ye, M. & Zhu, R. 2014 Facile preparation of mesoporous nickel oxide microspheres and their adsorption property for methyl orange from aqueous solution. *Materials Science in Semiconductor Processing* **26**, 716–725.

Jiang, R., Fu, Y. Q. & Zhu, H. Y. 2012 Removal of methyl orange from aqueous solutions by magnetic maghemite/chitosan nano composite films: adsorption kinetics and equilibrium. *Journal of Applied Polymer Science* **125**, E540–E549.

Jiang, T., Liang, Y. D., He, Y. J. & Wang, Q. 2015 Activated carbon/$NiFe_2O_4$ magnetic composite: a magnetic adsorbent for the adsorption of methyl orange. *Journal of Environmental Chemical Engineering* **3**, 1740–1751.

Körbahti, B. K., Artut, K., Geçgel, C. & Özer, A. 2011 Electrochemical decolorization of textile dyes and removal of metal ions from textile dye and metal ion binary mixtures. *Chemical Engineering Journal* **173**, 677–688.

Kuang, S. P., Wang, Z. .Z., Liu, J. & Wu, Z. C. 2013 Preparation of triethylene-tetramine grafted magnetic chitosan for adsorption of Pb(II) ion from aqueous solutions. *Journal of Hazardous Materials* **260**, 210–219.

Li, K., Li, P., Cai, J., Xiao, S., Yang, H. & Li, A. 2016 Efficient adsorption of both methyl orange and chromium from their aqueous mixtures using a quaternary ammonium salt modified chitosan magnetic composite adsorbent. *Chemosphere* **154**, 310–318.

Lian, L., Guo, L. & Guo, C. 2009 Adsorption of Congo red from aqueous solutions onto Ca-bentonite. *Journal of Hazardous Materials* **161**, 126–131.

Liu, X. Y., An, S. A. & Wang, Y. J. 2015 Rapid selective separation and recovery of a specific target dye from mixture consisted of different dyes by magnetic Ca-ferrites nanoparticles. *Chemical Engineering Journal* **262**, 517–526.

Ma, J., Yu, F., Zhou, L., Jin, L., Yang, M., Luan, J., Tang, Y., Fan, H., Yuan, Z. & Chen, J. 2012 Enhanced adsorptive removal of methyl orange and methylene blue from aqueous solution by alkali-activated multiwalled carbon nanotubes. *Applied Materials & Interfaces* **4** (11), 5749–5760.

Ma, Q., Shen, F. & Lu, X. 2013 Studies on the adsorption behavior of methyl orange from dye waste water onto activated clay. *Desalination and Water Treatment* **51**, 3700–3709.

Mekatel, E. H., Amokrane, S., Aid, A., Nibou, D. & Trari, M. 2015 Adsorption of methyl orange on nanoparticles of a synthetic zeolite NaA/CuO. *Comptes Rendus Chimie* **18**, 336–344.

Muthukumaran, C., Sivakumar, V. M. & Thirumarimurugan, M. 2016 Adsorption isotherms and kinetic studies of crystal violet dye removal from aqueous solution using surfactant modified magnetic nanoadsorbent. *Journal of the Taiwan Institute of Chemical Engineers* **63**, 354–362.

Reddy, D. H. K. & Lee, S.-M. 2013 Application of magnetic chitosan composites for the removal of toxic metal and dyes from aqueous solutions. *Advances in Colloid and Interface Science* **201–202**, 68–93.

Ren, Y., Abbood, H. A., He, F., Peng, H. & Huang, K. X. 2013 Magnetic EDTA-modified chitosan/SiO_2/Fe_3O_4 adsorbent: preparation, characterization, and application in heavy metal adsorption. *Chemical Engineering Journal* **226**, 300–311.

Sakkayawong, N., Thiravetyan, P. & Nakbanpote, W. 2005 Adsorption mechanism of synthetic reactive dye wastewater by chitosan. *Journal of Colloid and Interface Science* **286**, 36–42.

Sen, T. K., Afroze, S. & Ang, H. M. 2010 Equilibrium, kinetics and mechanism of removal of methylene blue from aqueous solution by adsorption onto pine cone biomass of *Pinus* radiate. *Water, Air & Soil Pollution* **218**, 499–515.

Subbaiah, M. V. & Kim, D. S. 2016 Adsorption of methyl orange from aqueous solution by aminated pumpkin seed powder: kinetics, isotherms, and thermodynamic studies. *Ecotoxicology and Environmental Safety* **128**, 109–117.

Tang, Y. J., Wang, X. & Zhu, L. Y. 2013 Removal of methyl orange from aqueous solutions with poly(acrylic acid-co-acrylamide) superabsorbent resin. *Polymer Bulletin* **70**, 905–918.

Wang, L., Ge, S. S. & Shao, Q. 2016 Preparation and adsorption properties of microspheres of ZnNiAl layered double hydroxides. *Chinese Journal of Inorganic Chemistry* **32**, 1896–1904.

Weng, C. H. & Pan, Y. F. 2007 Adsorption of a cationic dye (methylene blue) onto spent activated clay. *Journal of Hazardous Materials* **144**, 355–362.

Wu, T. H., Shao, Q., Ge, S. S., Bao, L. & Liu, Q. 2016 The facile preparation of novel magnetic zirconia composites with the aid of carboxymethyl chitosan and their efficient removal of dye. *RSC Advances* **6** (2016), 58020–58027.

Yagub, M. T., Sen, T. K. & Ang, H. M. 2012 Equilibrium, kinetics, and thermodynamics of methylene blue adsorption by pine tree leaves. *Water, Air & Soil Pollution* **223**, 5267–5282.

Zhang, G., Yi, L., Deng, H. & Sun, P. 2014 Dyes adsorption using a synthetic carboxymethyl cellulose-acrylic acid adsorbent. *Journal of Environmental Sciences* **26**, 1203–1211.

Zhu, H. Y., Jiang, R., Xiao, L. & Zeng, G. M. 2010 Preparation, characterization, adsorption kinetics and thermodynamics of novel magnetic chitosan enwrapping nanosized gamma-Fe_2O_3 and multi-walled carbon nanotubes with enhanced adsorption properties for methyl orange. *Bioresource Technology* **101** (14), 5063–5069.

First received 9 June 2017; accepted in revised form 15 November 2017. Available online 27 November 2017